Dalton Transactions

Accepted Manuscript

ROYAL SOCIETY OF CHEMISTRY

www.rsc.org/dalton

P(EO-*co*-LLA) Functionalized Fe_3O_4@$mSiO_2$ Nanocomposites for Thermo/pH Responsive Drug Controlled Release and Hyperthermia

Wei Guo[1], Chunyu Yang[1], Huiming Lin[1,2]* and Fengyu Qu[1]*

1 *Laboratory for Photon and Electronic Bandgap Materials, Ministry of Education, College of Chemistry and Chemical Engineering, Harbin Normal University, Harbin 150025, China.*
2 *Institute of Functional Material Chemistry, Faculty of Chemistry, Northeast Normal University, Changchun, 130024, P. R. China.*

Abstract

Fe_3O_4@$mSiO_2$ nanocarrier consisted of magnetic Fe_3O_4 nanoparticle core and mesoporous silica ($mSiO_2$) shell was synthesized. It shows uniform sphere morphology about 65 nm in diameter. Considering the magnetic hyperthermia of Fe_3O_4 under alternating magnetic field (AMF), a thermo-sensitive polymer poly [(ethylene glycol)-*co*-(L-lactide)] (P(EO-*co*-LLA)) was used as "gatekeeper" coating outside Fe_3O_4@$mSiO_2$ to regulate drug release behavior. The design of the nanocarrier was expected to block off the pores at low temperature and reopen at high temperature reversibly. The obtained hybrid nanocomposites were capable of loading anti-cancer drug doxorubicin (DOX) and controlled drug release behavior trigged by the hyperthermia of Fe_3O_4 under AMF. Besides, the nanocarriers also show pH-sensitive drug release based on the slight difference between tumor (weakly acid) and normal tissue (weakly alkaline). What's more, the chemotherapy of DOX combined with magnetic hyperthermia can improve the cytotoxicity obviously. On the

basis of the high stability and excellent controlled release performance, the multifunctional nanocarriers exhibit potential application on targeted-control drug release and hyperthermia for cancer treatment.

E-mail: *qufengyu2013@gmail.com* and *linhuiming@hrbnu.edu.cn*

Introduction

Cancer, which has been regarded as a major cause of mortality worldwide, is a huge group of diseases produced by rapid unregulated cell growth. And chemotherapy remains to be one of the most commonly used methods of many cancer treatments. To improve the therapy effect, nanomedicine has been employed as the platform, showing a good performance. To date, multifunctional nanoparticles, including polymers, micelles, liposomes, dendrimers, ceramics, and even virus capsids, have been used in medical diagnostics, drug delivery and therapy etc.[1–11] Among these, mesoporous silica nanoparticles (MSNs) have been considered as the most potential inorganic hosts to store and release drug molecules due to their excellent properties, such as uniform and tunable morphology and pore size, high pore volume and surface area, easily modified surface properties, good biocompatibility and biodegradation.[12–16]

However, without the specific discrimination between normal cell and cancer cell, chemotherapy always induces a huge side effect besides the efficacy. To obtain a smart drug release behavior and beneficial therapy effect, much attention has been focused on the mesoporous silica nanocontainers equipped with “gatekeepers” as the delivery vehicles, in which a regulated drug release at specific time interval and targeted site can be achieved by taking advantage of various “gatekeepers”.[17–19] Currently, nanoparticles, organic molecules and supramolecular nanovalves have been employed as “gatekeepers” for MSNs, and the controlled release process can be regulated by many special stimulus, such as thermal/electrostatics/magnetic actuation,

light, photoirradiation, pH and enzymes.[20–26] For example, using DNA block copolymers as capping agent, Herrmann et al. realized light-triggered targeted cargo release.[27] In our previous study, Konjac oligosaccharide (KOGC) was adopted as the "gatekeeper". Owing to the degradation of "gate" (KOGC), the cargos can be released triggered by β-mannanase, a normal enzyme in colon of the human body.[28]

Magnetic (Fe_3O_4 or γ-Fe_2O_3) nanoparticles with strong magnetic property and low toxicity have been widely used as targeted and magnetic resonance imaging agents.[29–31,33] For example, Wang and coworkers synthesized a bicontrollable drug release system with PAH/PSS multilayers on to Fe_3O_4/mSiO_2, showing the magnetic-targeted and pH-controllable release behavior.[32] Ultra-small γ-Fe_2O_3 nanoparticles also have been described as the potential specific positive contrast agents for magnetic resonance molecular imaging.[33-35] Moreover, magnetic nanoparticles can produce localized hyperthermia by hysteresis heating upon exposure to an alternating magnetic field (AMF).[36] When the temperature is raised to 42-45 °C, tumor/cancer cells are damaged or killed due to overheating, while most of the normal cells which far away from the magnetic nanoparticles survive.[37,38] Presently, there are few reports about the combination of hyperthermia with thermo-sensitive controlled release.[39,40] Vallet-Regí et al. synthesized mesoporous silica nanoparticles with iron oxide nanocrystals encapsulated inside the silica matrix and decorated on the surface with a thermoresponsive copolymer of poly(ethyleneimine)-b-poly(N-isopropylacrylamide) (PEI/NIPAM).[41] Lin and coworkers prepared multifunctional nanocarriers based on the up-conversion

luminescent nanoparticles and thermo/pH-coupling sensitive polymer poly[(N-isopropylacrylamide)-co-(methacrylic acid).[42]

Herein, the core-shell nanomaterial (Fe_3O_4@$mSiO_2$), with magnetic Fe_3O_4 nanoparticles as core and mesoporous silica as shell, was synthesized as the drug loading host. Poly [(ethylene glycol)-*co*-(L-lactide)] (P(EO-*co*-LLA)) was chosen to graft outside Fe_3O_4@$mSiO_2$ as blocking caps. It is known that P(EO-*co*-LLA) is a typical thermo-sensitive polymer, which exhibits reversible phase transitions between sol and gel in aqueous solution based on the change of the temperature.[43] And the hyperthermia of Fe_3O_4 can be served as the "trigger" to control "on-off" of the thermo sensitive polymer which is capable of regulate the drug release. From Scheme 1, firstly, Fe_3O_4@$mSiO_2$ nanomaterials were synthesized by using the typical stöber method. After the modification of Fe_3O_4@$mSiO_2$ with -COOH, P(EO-*co*-LLA) can be grafted onto Fe_3O_4@$mSiO_2$ as the "gatekeeper". Doxorubicin hydrochloride (DOX) was adopted as the model to investigate the drug release kinetics of the system. Beside the thermo-sensitive control release behavior triggered by the hyperthermia of Fe_3O_4, the nanocarriers also show the pH-sensitive control release based on the slight acidity difference between the tumor and the normal tissue. The magnetic hyperthermia assisted–thermo/pH drug release can improve the therapeutic effect on tumor treatment.

Experimental Section

Materials

Unless specified, all the chemicals were analytical grade and used without further

purification. Cetyltrimethylammonium bromide (CTAB), Tin(II) 2-ethylhexanoate, 3-aminopropyltriethoxysilane (APTES), tetraethyl orthosilicate (TEOS), 3-[4,5-dimethylthialzol-2-yl]-2,5-diphenyltetrazolium bromide (MTT), 2'-(4-Ethoxyphenyl)-5-(4-methyl-1-piperazinyl)-2,5'-bi-1*H*-benzimidazole, trihydrochloride (Hoechst 33342), and monomethoxy poly(ethylene oxide) (PEO, Mn ~5000), were purchased from Sigma-Aldrich. L-lactide (LLA) was purchased from Changchun SinoBiomaterials Co. Ltd.. Doxorubicin hydrochloride (DOX), sodium oleate and oleic acid were obtained from Aladdin, China. Dimethyl sulfoxide, ferric trichloride hexahydrate ($FeCl_3 \cdot 6H_2O$), ethanol, n-hexane and triethylamine were purchased from Tianjin Chemical Corp. of China.

Synthesis of Fe_3O_4 Nanoparticles

In a typical synthesis of iron–oleate complex, 10.8 g of iron chloride ($FeCl_3 \cdot 6H_2O$, 40 mmol) and 36.5 g of sodium oleate (120 mmol, 95%) were dissolved in a mixture solvent composed of 80 mL ethanol, 60 mL distilled water and 140 mL hexane. The resulting solution was heated to 70 °C and kept at that temperature for four hours. When the reaction was completed, the upper organic layer containing the iron-oleate complex was washed three times with 30 mL distilled water in a separatory funnel. After washing, hexane was evaporated, resulting in an iron-oleate complex in a waxy solid form.

Following a literature procedure, Fe_3O_4 nanoparticles were prepared.[44] 36 g (40 mmol) of the iron-oleate and 5.7 g of oleic acid (20 mmol, 90%) were dissolved in 200 g of 1-octadecene (90%) at room temperature. The reaction mixture was heated to

320 °C at a constant heating rate of 3.3 °C min^{-1}, and then kept at that temperature for 30 min. When the reaction temperature reached 320 °C, a severe reaction occurred and the initial transparent solution became turbid and brownish black. The resulting solution containing the nanocrystals was then cooled to room temperature, and 500 mL of ethanol was added to the solution to precipitate the nanocrystals, which were further collected by centrifugation and then dispersed in chloroform.

Synthesis of Fe_3O_4@mSiO_2 Nanoparticles

In a typical procedure, 0.5 mL of the Fe_3O_4 nanocrystals in chloroform (10 mg mL^{-1}) was poured into 8 mL of a 0.2 M aqueous CTAB solution and the resulting solution was stirred vigorously for 30 min. The formation of an oil-in-water microemulsion resulted in a turbid brown solution. Then, the mixture was held at 60 °C for 30 min to evaporate the chloroform, resulting in a transparent black Fe_3O_4/CTAB solution. Then, 20 mL of distilled water was added to the obtained black solution and the pH value of the mixture was adjusted to 8 to 9 by using 0.1 M NaOH. After that, 100 μL of 20 % TEOS in ethanol was injected six times in 30 min intervals. The reaction mixture was reacted for 24 h under vigorous stirring. The as-synthesized Fe_3O_4@mSiO_2 NPs were washed 3 times with ethanol to remove the unreacted species.

Syntheses of Diblock Copolymers (P(EO-*co*-LLA)) with Different Molecular Weights

P(EO-*co*-LLA)-7,250 was synthesized following a literature procedure,[45] PEO (8 g, 1.60 mmol) was added to 80 mL of dried toluene and the residual water in the solution was removed by azeotropic distillation to a final volume of 30 mL. L-lactide (3.6 g,

25.00 mmol) and stannous octoate (8.7 mg, 21.47 mmol) were added to this PEO/toluene solution and refluxed under dry nitrogen atmosphere for 24 h. The solution was precipitated in diethyl ether, filtered, and the residual solvent was eliminated by vacuum. Diblock copolymers with various molecular weight P(EO-*co*-LLA)-8,750 and P(EO-*co*-LLA)-10,000 were synthesized by the similar method with 6 g and 8 g of L-lactide. The NMR spectrum of as-synthesized P(EO-*co*-LLA) is shown in Fig. S1 that testifies the polymerized between PEO and L-lactide.

Synthesis of Fe_3O_4@mSiO_2-P(EO-*co*-LLA)

In a typical procedure, as-synthesized Fe_3O_4@mSiO_2 nanoparticles (300 mg) were suspended in 20 mL of dry toluene containing 100 μL of APTES. The solution was stirred at 50 °C under nitrogen for 4 h to obtain amine-functionalized Fe_3O_4@mSiO_2 (Fe_3O_4@mSiO_2-NH_2). Later on, 200 mg of Fe_3O_4@mSiO_2-NH_2 was added into 10 mL DMSO solution containing succinic anhydride (60 mg) and triethylamine (60 mg) and stirred at 40 °C for 48 h to produce the carboxyl-functionalized Fe_3O_4@mSiO_2 (Fe_3O_4@mSiO_2-COOH). 330 mg of Fe_3O_4@mSiO_2-COOH was added into 20 mL methylene chloride solution containing 350 mg of dichlorosulfoxide and stirred at 50 °C for 4 h, and then 4.0 g of P(EO-*co*-LLA) (Mn = 7,250) was added and stirred for another 4 h to obtain Fe_3O_4@mSiO_2-P7,250. Using P(EO-*co*-LLA)s with other molecular weight (8,750 and 10,000), the samples were named as Fe_3O_4@mSiO_2-P8,750 and Fe_3O_4@mSiO_2-P10,000.

Preparation of FITC labeled Fe_3O_4@mSiO_2-P(EO-*co*-LLA).

In a typical synthesis of FITC-APTES, 15.6 mg of FITC and 100 μL of (3-aminopropyl)triethoxysilane (APTES) were dissolved in 5 mL DI water. The resulting solution was stirred at room temperature and kept in dark for 24 hours. FITC-APTES is attached to Fe_3O_4@mSiO_2-P(EO-*co*-LLA) via the reaction among silica coupling groups of FITC-APTES and the residual Si-OH on the silica spheres. In a typical process, 60.0 mg of Fe_3O_4@mSiO_2-P(EO-*co*-LLA) was dispersed in 3 mL of DI water, and then 2 mL of obtained FITC-APTES solution was added. The reaction was performed in dark at ambient temperature overnight. The solid was collected by centrifugation followed by washing with DI water for 6 times and then freeze drying.

Drug Loading and Release

Fe_3O_4@mSiO_2-P(EO-*co*-LLA) (60 mg) was added to the DOX solution (3 mL, 1 mg mL^{-1}) and stirred at 45 °C for 12 h. And then, the solid was shock cooled, centrifuged, and washed several times with distilled water. The loading amount of DOX was determined by the UV/vis spectroscope at 480 nm, and the drug loading sample was named as DOX-Fe_3O_4@mSiO_2-P(EO-*co*-LLA). The loading efficiency (LE %) of DOX can be calculated by using the formula (1). The experiment was repeated three times.

$$LE\% = \frac{m_{(\text{original DOX})} - m_{(\text{residual DOX})}}{m_{(mSiO_2)} + m_{(\text{original DOX})} - m_{(\text{residual DOX})}} \times 100\% \quad (1)$$

The gating protocol was investigated by studying the release profiles of DOX from the DOX-Fe_3O_4@mSiO_2-P(EO-*co*-LLA), at 25/45 °C in certain media solution (pH

5.8 or 7.4, phosphate buffer solution). Briefly, 10 mg of DOX loaded Fe_3O_4@mSiO_2-P(EO-*co*-LLA) (DOX-Fe_3O_4@mSiO_2-P(EO-*co*-LLA)) was dispersed in 5 mL of media solution and sealed in a dialysis bag (molecular weight cutoff 8000), which was submerged in 20 mL of media solution. At selected intervals, the solution was taken out to determine the release amount by UV. The drug release of DOX from the DOX-Fe_3O_4@mSiO_2-P(EO-*co*-LLA) in AMF experiments was performed with the similar method, but the difference is that the drug loading system was put in the AC magnetic field(250 KHz).

Cell Culture

HeLa cells (cervical cancer cell line) were grown in a monolayer of Dulbecco's Modified Eagle's Medium (DMEM, Gibco) supplemented with 10% (v/v) fetal bovine serum (FBS, Tianhang Bioreagent Co., Zhejiang) and penicillin/streptomycin (100 U mL^{-1} and 100 μg mL^{-1}, respectively, Gibco) in a humidified 5% CO_2 atmosphere at 37 °C.

Confocal Laser Scanning Microscopy (CLSM)

To determine the cellular uptake, HeLa cells were cultured in a 12-well chamber slide with one piece of cover glass at the bottom of each chamber in the incubation medium (DMEM) for 24 h. The cell nucleus was labeled with Hoechst 33342. Fe_3O_4@mSiO_2-P(EO-*co*-LLA) was added to the incubation medium at a concentration of 100 μg mL^{-1} for 6 h of incubation in 5% CO_2 at 37 °C. After the medium was removed, the cells were washed twice with PBS (pH 7.4) and the cover glass was visualized under a laser scanning confocal microscope (FluoView FV1000,

Olympus).

Cell Viability

The viability of cells in the presence of nanoparticles was investigated using a 3-[4,5-dimethylthialzol-2-yl]-2,5-diphenyltetrazolium bromide (MTT, Sigma) assay. The assay was performed in triplicate in the following manner. For the MTT assay, HeLa cells were seeded into 96-well plates at a density of 1×10^4 per well in 100 μL of the medium and grown overnight. The cells were then incubated with various concentrations of the need tested samples for 48 h. Afterwards, cells were incubated in media containing 0.5 mg mL^{-1} of MTT for 4 h. The precipitated formazan violet crystals were dissolved in 100 μL of 10% SDS in 10 mmol HCl solution at 37 ℃ overnight. The absorbance was measured at 570 nm with a multidetection microplate reader (SynergyTM HT, BioTek Instruments Inc, USA).

Characterization

Powder X-ray patterns (XRD) were recorded on a Siemens D 5005 X-ray diffractometer with Cu Kα radiation (40 kV, 30 mA). The nitrogen adsorption/desorption, surface areas, and median pore diameters were measured using a Micromeritics ASAP 2010 M sorptometer. The surface area was calculated according to the conventional BET method and the adsorption branches of the isotherms were used for the calculation of the pore parameters using the BJH method. Fourier transform infrared (FTIR) spectra were recorded on a PerkinElmer 580B infrared spectrophotometer using the KBr pellet technique. A UV-vis spectrum was used to describe the amount of drug released (Shimadzu UV2550 spectrophotometer).

Transmission electron microscopy (TEM) images were recorded on a TECNAI F20. Zeta potential and dynamic light scattering (DLS) was carried out with ZetaPALS zeta potential annlyzer. The magnetic properties of samples were characterized with a vibrating sample magnetometer (Lake Shore 7410). The alternating magnetic field was generated by the alternating magnetic field (Generator-SP04C).

Results and Discussion

Morphology, Structure and Phase

TEM was used to display the core-shell structure of the samples (Fig. 1). Fig. 1A shows the TEM image of Fe_3O_4 nanoparticles that reveals a uniform and well dispersed spherical morphology with an average diameter of 20 nm in size. Fe_3O_4@$mSiO_2$ shows the obvious core-shell structure with Fe_3O_4 core and mesoporous silica shell about 20 nm in thickness (Fig. 1B). Through a esterification, P(EO-*co*-LLA) can be gated onto the surface of Fe_3O_4@$mSiO_2$. The polymer layers result in the rough surface and less dispersion of all Fe_3O_4@$mSiO_2$-P(EO-*co*-LLA) nanoparticles (Fig. 1C-E). Additionally, the hydrodynamic diameter of Fe_3O_4@$mSiO_2$ and Fe_3O_4@$mSiO_2$-P(EO-*co*-LLA)s were measured by Zeta Potential Analyzer. As illustrated in Fig. 1F, the diameter of Fe_3O_4@$mSiO_2$ centers at 82 nm that is larger than that observed from TEM because of the hydrate layer in aqueous environment. As depicted in Fig. 1G-I, the diameter of Fe_3O_4@$mSiO_2$-P(EO-*co*-LLA)s increase from 103 nm to 121 and 135 nm with the polymer molecular weight increase from 7,250 to 8,750 and 10,000, respectively. The zeta-potential test was further used to monitor the difference between Fe_3O_4@$mSiO_2$ and Fe_3O_4@$mSiO_2$-P(EO-*co*-LLA)s

(Fig. 2). The zeta-potential value increased from -16.02 ± 2.17 mV of Fe_3O_4@$mSiO_2$ to -2.2 ± 4.57 mV of Fe_3O_4@$mSiO_2$-P7,250. With abundant surface Si-OH, silica always shows the negative charge (-16.02 ± 2.17 mV). And after grafting with P(EO-*co*-LLA), the decrease of surface Si-OH induce the increase of zeta-potential for Fe_3O_4@$mSiO_2$-P(EO-*co*-LLA). Fe_3O_4@$mSiO_2$-P8,750 and Fe_3O_4@$mSiO_2$-P10,000 shows the zeta-potential of -3.08 ± 4.17 mV and -4.83 ± 5.86 mV, respectively (Fig. 2). Furthermore, with the same addition amount of P(EO-*co*-LLA), P(EO-*co*-LLA)-7,250 possesses the most molecules to interact with surface Si-OH and to make the highest zeta-potential of all.

Eager to further verify the successful grafting of P(EO-*co*-LLA) on Fe_3O_4@$mSiO_2$, FT-IR spectroscopy was monitored to study the organic and inorganic components of the samples.. The corresponding FT-IR spectra of PEO, L-lactide, P(EO-*co*-LLA), Fe_3O_4@$mSiO_2$ and Fe_3O_4@$mSiO_2$-P(EO-*co*-LLA) are shown in Fig. 3. As depicted in Fig. 3A, the absorption bands at 2948 and 2887 cm^{-1} are assigned to the C-H stretching vibrations, and the absorption bands at 1110 and 962 cm^{-1} can be assigned to the C-O-C stretching vibration and C-H rocking vibration of PEO. The obvious absorption band at 1762 cm^{-1} testifies the C=O stretching vibration of the ester group in L-lactide. In addition, L-lactide also gives the characteristic absorption bands at 935 and 656 cm^{-1} due to its six-membered ring structure. After the polymerization, P(EO-*co*-LLA) also shows the stretching vibration adsorption peaks of C=O (1758 cm^{-1}) and C-O-C (1110 cm^{-1}), but the six-membered rings characteristic absorption bands (935 and 656 cm^{-1}) disappear, testifying the open-ring polymerization of

L-lactide. In Fig. 3B, the obvious absorption band at 1086 cm^{-1} testifies the Si-O-Si framework of the Fe_3O_4@$mSiO_2$. After P(EO-*co*-LLA) grafted, two peaks assigned to C-H stretching vibrations at 2982 and 2938 cm^{-1} appears. And the absorption peaks at 1758, 1693 and 1639 cm^{-1} assigned to the C=O stretching vibration of P(EO-*co*-LLA) also can be found in Fe_3O_4@$mSiO_2$-P(EO-*co*-LLA), confirming that P(EO-*co*-LLA) has been successfully grafted on Fe_3O_4@$mSiO_2$.

The X-ray diffraction patterns (XRD) collected from Fe_3O_4@$mSiO_2$ and Fe_3O_4@$mSiO_2$-P(EO-*co*-LLA)s. In Fig. S2, all samples show only one diffraction peak at about 2 θ = 2.26°, suggesting they possesses the ordered mesoporous structure. It is clearly observed that the relative intensities of the peaks of the pattern collected from Fe_3O_4@$mSiO_2$-P(EO-*co*-LLA)s reduced obviously compared to that of Fe_3O_4@$mSiO_2$ without P(EO-*co*-LLA) grafted. Moreover, the larger the amount of P(EO-*co*-LLA) grafted onto Fe_3O_4@$mSiO_2$, the lower the diffraction intensity of Fe_3O_4@$mSiO_2$-P(EO-*co*-LLA)s, which is consistent with the previous report.[28] The pore structure and related textural properties of Fe_3O_4@$mSiO_2$ and Fe_3O_4@$mSiO_2$-P(EO-*co*-LLA)s were followed by nitrogen adsorption-desorption measurements. As can be seen in Fig. S3A, Fe_3O_4@$mSiO_2$ displays the typical IV adsorption isotherm and a steep capillary condensation step at P/P_0 = 0.2-0.4. The typical H4 hysteresis loop further testifies the mesoporous structure of Fe_3O_4@$mSiO_2$. As depicted in Figure S3A, there is much smaller uptakes of nitrogen for Fe_3O_4@$mSiO_2$-P(EO-*co*-LLA) if taking its counterpart (Fe_3O_4@$mSiO_2$) as a comparison. Additionally, the surface area (S_{BET}) and pore volume are reduced from

326 m^2 g^{-1} and 0.285 cm^3 g^{-1} for Fe_3O_4@$mSiO_2$ to 152 m^2 g^{-1} and 0.156 cm^3 g^{-1} for Fe_3O_4@$mSiO_2$-P7,250, 100 m^2 g^{-1} and 0.133 cm^3 g^{-1} for Fe_3O_4@$mSiO_2$-P8,752, 68.0 m^2 g^{-1} and 0.095 cm^3 g^{-1} for Fe_3O_4@$mSiO_2$-P10,000 (Table 1).

The magnetization characterization of the samples also was studied. Fig. 4 presents the magnetic hysteresis loop of Fe_3O_4 and Fe_3O_4@$mSiO_2$-P(EO-*co*-LLA) at room temperature. In Fig. 4, Fe_3O_4 nanoparticles possess magnetism with the saturation magnetizations (*M*s) about 80.5 emu g^{-1}. Fe_3O_4@$mSiO_2$-P(EO-*co*-LLA)s remain the super-paramagnetism with reduced *M*s about 59.5, 55.6, and 48.7 emu g^{-1}, which is ascribed to the nonmagnetic $mSiO_2$ and P(EO-*co*-LLA).

Drug loading and release profiles

To investigate the sensitive and controlled release properties of Fe_3O_4@$mSiO_2$-P(EO-*co*-LLA)s, DOX was selected as the model drug and the release performances were investigated in detail (Table 1). The actual loading levels of DOX are calculated to be 6.8 ± 0.5, 6.2 ± 0.6 and 5.9 ± 0.4 % with the increase of the corresponding molecular weight of P(EO-*co*-LLA)s from 7,250 to 8,750 and 10,000, respectively. It is known that, the drug loading ability is related to the surface area of carriers. With a large surface area, Fe_3O_4@$mSiO_2$-P7,250 (152 m^2 g^{-1}) possesses a high drug loading amount (6.8 ± 0.5%).

The release profiles of DOX-Fe_3O_4@$mSiO_2$-P(EO-*co*-LLA)s in PBS buffer (pH 7.4) in response to the temperature (20 and 45 ° C) are shown in Fig. 5A. In Fig. 5A (d-e), all samples show low release cumulative amount (below 10 %) until 24 h at the low temperature (25 °C). However, the release became more easily when the temperature

increased to 45 °C. In Fig. 5A (a-c), the cumulative release amount of DOX reaches 24.7, 28.6 and 38.0 % for DOX-Fe_3O_4@mSiO_2-P7,250, DOX-Fe_3O_4@mSiO_2-P8,750 and DOX-Fe_3O_4@mSiO_2-P10,000 within 24 h, respectively. With a higher molecular weight of the polymer, DOX-Fe_3O_4@mSiO_2-P10,000 shows a higher release amount (38.0 %).

Considering the pH-sensitivity of P(EO-*co*-LLA), the release profiles of DOX-Fe_3O_4@mSiO_2@P10,000 was also studied at different pH condition (pH 7.4, 5.8 and 4.0). In Fig. 5B, the fast burst release can be found at pH 4. It just takes 24 h to reach maximum release (92.7 %). However, when the pH value increases to 5.8, the release rate decreases as well as the release amount. Fig. 5B shows about 89.4 % release amount until 24 h at pH 5.8. Going on to increase the pH value to 7.4, the release decreases more obviously (38.0 %). From the above, the acid condition is benefit for the drug release. Comparing the release profiles in Fig. 5B and C, it can be also found that the release at 45 °C is freer than that at 25 °C.

To further reveal the sensitive-release mechanism of the system, the hydrodynamic sizes of all samples under different temperature/pH value/molecular amount were investigated and summarized in Table 2. As can be seen in Table 2, as the molecular amount of P(EO-*co*-LLA)s increases from 7,250 to 8,750 and 10,000, the hydrodynamic size of Fe_3O_4@mSiO_2-P(EO-*co*-LLA)s increases from 108 to 149 nm at pH 7.4 (25 °C). With the high molecular amount of P(EO-*co*-LLA), the corresponding hydrodynamic size increases due to the long chain of the polymer brushes that makes the release amount decrease from 10.1 % of

DOX-Fe_3O_4@mSiO_2-P7,250 to 7.1 % of DOX-Fe_3O_4@mSiO_2-P10,000 (Fig. 5A).

It is known that P(EO-*co*-LLA) is a typical temperature sensitive polymer, which can change from sol to gel as the temperature increase above its lower critical solution temperature (LCST). As displayed in Table 2, when the temperature increases to 45 °C, the hydrodynamic size of Fe_3O_4@mSiO_2-P(EO-*co*-LLA)s deceases to 102, 122, and 138 nm (pH 7. 4) due to the shrink of the polymer brushes at high temperature. In short, when the temperature increases to 45 °C, all the releases were accelerated and the release amount increased obviously, while at 25 °C, the loose polymer brushes block the pore and make the release below 10 %. Furthermore, the shrink/loose of polymer brushes based on temperature takes place not only at pH 7.4, but also at pH 5.8 and 4.0 (Table 2).

As mentioned above, beside the temperature-triggered release, DOX-Fe_3O_4 @mSiO_2-P10,000 also reveals the pH sensitive-release behavior under different pH condition. It is known that, the swelling of P(EO-*co*-LLA) in aqueous solution depends on the hydrogen bond between P(EO-*co*-LLA) and H_2O. When decreasing the pH value of the solution, the hydrogen bond is weakened leading to the polymer brushes shrink. As illustrated in Table 2, as the pH value decreases from 7.4 to 5.8 and 4.0, the hydrodynamic size of DOX-Fe_3O_4@mSiO_2-P10,000 decreases from 149 to 131 and 128 nm at 25 °C and from 138 to 105 and 99 nm at 45 °C. So that, the shrink of P(EO-*co*-LLA) makes the preponderant release in acid environment as depicted in Fig. 5B and C.

From the above investigation, the temperature-triggered release behavior of the

nanocomposites is very definite. Considering the hyperthermia of the magnetic Fe_3O_4, AMF was also introduced to control the release process and the release performances. As shown in Fig. 5D, under the stimulus of AMF, the release is enhanced to 28.7 % at 2 h and 89.4 % at 12 h. To further reveal the AMF enhanced release, the release without AMF first and then with AMF was also carried out. And the release is very slow about 7.8 % at the first 2 h. And then, AMF was introduced and the release increased to 41.3 % at 4h and even 86.8 % at 12 h. In addition, the time-dependent temperature of Fe_3O_4@mSiO_2-P10,000 under AMF treatment is shown in Fig. S4. After AMF treatment for 10 min, the temperature increases to 35 °C. And it costs about 20 min to reach 45 °C. With time going on, the temperature can reach 47°C under the AMF stimulus for 30 min. In Fig. 5D and S4, AMF stimuli-release can be ascribed to the hyperthermia of the magnetic Fe_3O_4 that makes the temperature increase and drug release.

In vitro Cytotoxic Effect and Cellular Uptake

To investigate the cellular uptake of the sample, DOX-Fe_3O_4@mSiO_2-P10,000 was incubated with HeLa cells at the concentration of 100 μg mL^{-1} for 6 h. The cellular uptake and subsequent localization of the sample is shown in Fig. 6. As can be seen in Fig. 6, nanoparticles are localized in the cytoplasm after 6 h incubation, proving the fast cellular uptake of the sample. In addition, DOX can be found in karyon that is because the nanocomposites were taken into the cytoplasm and the low-pH endosomal environment induced the drug release.[15]

To compare the anticancer efficacy of the DOX-loaded nanocomposites and free

DOX, HeLa cells were incubated in culture medium in the presence of free DOX, Fe_3O_4@mSiO_2-P10,000 and DOX-Fe_3O_4@mSiO_2-P10,000 with various concentrations for 48 h, and then MTT assay was used for quantitative testing of the cell viability. As shown in Fig. 7A, Fe_3O_4@mSiO_2 -P10,000 shows high cell viability (89.5%) even after 48 h incubated with the sample concentration as high as 480 μg mL^{-1}, showing neglectable toxicity and well biocompatibility of the nanocomposites. However, the cell viability decreases to 62.7 % (480 μg mL^{-1}) due to the hyperthermia of the magnetic nanocomposites under AMF treatment (Fig. 7A).

In Fig. 7B, DOX-Fe_3O_4@mSiO_2-P10,000 exhibits 71.5 % apoptosis at an equivalent DOX concentration of 50 μg mL^{-1}. Assisted with AMF stimulus, the cellular apoptosis enhanced to 93.7 %, revealing that the chemotherapy combined with hyperthermia can improve the cellular cytotoxicity obviously. Furthermore, free DOX exhibits slightly higher cytotoxicity than DOX-Fe_3O_4@mSiO_2-P10,000 at low concentrations region. However, that was inversed when the concentration of DOX is up to 12.5 μg mL^{-1}. Because the small molecules like DOX can diffuse into cells rapidly that induces the high cytotoxicity for free DOX at low concentration. Whereas the cytotoxicity of DOX-Fe_3O_4@mSiO_2-P10,000 derived from the released DOX molecules after endocytic uptake by cancer cells.[46] At high concentration, the high uptake of the nanocomposites by HeLa cells through endocytosis, followed by the low-pH induced release of the loaded DOX inside the endosomal compartment, making the higher cytotoxicity of DOX-Fe_3O_4@mSiO_2-P10,000 than free DOX molecules. In addition, the chemotherapy combined with the hyperthermia makes

DOX-Fe_3O_4@mSiO_2-P10,000 show the obvious enhanced cytotoxicity (93.7 %) as an equivalent DOX (87.4 %) concentration of 50 μg mL^{-1}.

Conclusion

In summary, Fe_3O_4@mSiO_2 core-shell nanocomposites were synthesized as the nanocarriers. And, considering the magnetic hyperthermia of Fe_3O_4 under AMF, a thermo-sensitive polymer P(EO-*co*-LLA) was used as "gatekeeper" coating outside Fe_3O_4@mSiO_2 to regulate the drug release behavior. After the loading of anticancer drug DOX, the composites show the controlled drug release behavior trigged by the hyperthermia of Fe_3O_4 under AMF. Beside this, the nanocarriers also demonstrate the pH-sensitive control release based on the slight acidity difference between the tumor and the normal tissue. The chemotherapy of anticancer drug combined with magnetic hyperthermia enhances the cytotoxicity obviously. Therefore, with these unique properties, the nanocomposites possess potential application in targeted-control drug release and hyperthermia for cancer therapy.

Acknowledgments

Financial support for this study was provided by the National Natural Science Foundation of China (21171045, 21101046), Natural Science Foundation of Heilongjiang Province of China ZD201214，Program for Scientific and Technological Innovation team Construction in Universities of Heilongjiang province (2011TD010), Technology development pre-project of Harbin Normal University (12XYG-11), and China Postdoctoral Science Foundation (2013M541265).

References

1 B. Fischer, P. Heffeter, K. Kryeziu, L. Gille, S. M. Meier, W. Berger, C. R. Kowol and B. K. Keppler, *Dalton Trans.*, 2014, **43**, 1096.

2 J. Wu, Y. J. Zhu, F. Chen, X. Y. Zhao, J. Zhao and C. Qi, *Dalton Trans.*, 2013, **42**, 7032.

3 X. Q. An, F. Zhan and Y. Y. Zhu, *Langmuir*, 2013, **29**, 1061.

4 J. C. Fernandes, X. P. Qiu, F. M. Winnik, M. Benderdour, X. Zhang, K. Dai and Q. Shi, *Internat. J. Nanomedicine*, 2012, **7**, 5833.

5 A. Shimoda, S. I. Sawada, A. Kano, A. Maruyama, A. Moquin, F. M. Winnik and K. Akiyoshi, *Colloid. Surface. B.*, 2012, **99**, 38.

6 E. R. Gillies and J. M. Fréchet, *Drug. Discovery. Today.*, 2005, **10**, 35.

7 M. Colilla, B. González and M. Vallet-Regí, *Biomater. Sci.*, 2013, **1**, 114.

8 M. Vallet-Regí and E. Ruiz-Hernández, *Adv. Mater.*, 2011, **23**, 5177.

9 J. Chang, Y. Li, G. Wang, B. He and Z. W. Gu, *Nanoscale*, 2013, **5**, 813.

10 A. H. Faraji and P. Wipf, *Bioorg. Med. Chem.*, 2009, **17**, 2950.

11 H. Y. Chen, B. W. Li, J. D. Qiu, J. Y. Li, J. Jin, S. H. Dai, Y. X. Ma and Y. Q. Gu, *Nanoscale*, 2013, **5**, 12409.

12 H. Kim, S. Kim, C. Park, H. Lee, H. J. Park and C. Kim, *Adv. Mater.*, 2010, **22**, 4280.

13 Y. N. Zhao, B. G. Trewyn, I. I. Slowing and V. S-Y. Lin, *J. Am. Chem. Soc.*, 2009, **131**, 8398.

14 H. S. Park, C. W. Kim, H. J. Lee, J. H. Choi, S. G. Lee, Y. P. Yun, I. C. Kwon, S. J.

Lee, S. Y. Jeong and S. C. Lee, *Nanotechnology*, 2010, **21**, NO. 225101.

15 L. Yuan, Q. Tang, D. Yang, J. Z. Zhang, F. Zhang and J. Hu, *J. Phys. Chem. C.*, 2011, **115**, 9926.

16 X. F. Guo, Y. S. Kim and G. J. Kim, *J. Phys. Chem. C.*, 2009, **113**, 8313.

17 X. Zhang, P. P. Yang, Y. L. Dai, P. A. Ma, X. J. Li, Z. Y. Cheng, Z. Y. Hou, X. J. Kang, C. X. Li and J. Lin, *Adv. Funct. Mater.*, 2013, **23**, 4067.

18 Z. Li, J. L. Nyalosaso, A. A. Hwang, D. P. Ferris, S. Yang, G. Derrien, C. Charnay, J. O. Durand and J. I. Zink, *J. Phys. Chem. C.*, 2011, **115**, 19496.

19 J. T. Sun, C. Y. Hong and C. Y. Pan, *J. Phys. Chem. C.*, 2010, **114**, 12481.

20 M. W. Ambrogio, C. R. Thomas, Y-L. Zhao, J. I. Zink and J. F. Stoddart, *Acc.Chem. Res.*, 2011, **44**, 903.

21 S. Angelos, N. M. Khashab, Y. W. Yang, A. Trabolsi, H. A. Khatib, J. F. Stoddart and J. I. Zink, *J. Am. Chem. Soc.*, 2009, **131**, 12912.

22 D. P. Ferris, Y. L. Zaho, N. M. Khashab, H. A. Khatib, J. F. Stoddart and J. I. Zink, *J. Am. Chem. Soc.*, 2009, **131**, 1686.

23 E. Aznar, M. D. Marcos, R. Martinez-Manez, F. Sancenon, J. Soto, P. Amoros and C. Guillem, *J. Am. Chem. Soc.*, 2009, **131**, 6833.

24 Y. Zhu, W. Meng, H. Gao and N. Hanagata, *J. Phys. Chem. C.*, 2011, **115**, 13630.

25 S. Angelos, E. Choi, F. Vögtle, L. De Cola and J. I. Zink, *J. Phys. Chem. C.*, 2007, **111**, 6589.

26 X. R. Zhang, D. Chabot, Y. Sultan, C. Monreal and M. C. DeRosa, *ACS Appl. Mater. Interfaces*, 2013, **5**, 5500.

27 A. Rodríguez-Pulido, A. I. Kondrachuk, D. K. Prusty, J. Gao, M. A. Loi and A. Herrmann, *Angew. Chem. Int. Ed.*, 2013, **52**, 1008.

28 W. Guo, C. Y. Yang, L. R. Cui, H. M. Lin and F. Y. Qu, *Langmuir*, 2014, **30**, 243.

29 R. Weissleder, A. Bogdanov, E. A. Neuwelt and M. Papisov, *Adv. Drug Del. Rev.*, 1995, **16**, 321.

30 J. Su, M. Cao, L. Ren and C. Hu, *J. Phys. Chem. C.*, 2011, **115**, 14469.

31 X. Li, X. Huang, D. Liu, X. Wang, S. Song, L. Zhou and H. Zhang, *J. Phys. Chem. C.*, 2011, **115**, 21567.

32 R. Xu, G. Y. Sun, Q. Y. Li, E. B. Wang and J. M. Gu, *Solid. State. Sci.*, 2010, **12**, 1720.

33 E. Taboada, E. Rodríguez, A. Roig, J. Oró, A. Roch and R. N. Muller, *Langmuir*, 2007, **23**, 4583.

34 V. Rocher, J. Manerova, M. Kinnear, D. J. Evans and M. G. Francesconi, *Dalton Trans.*, 2014, **43**, 2948.

35 T. D. Schladt, K. Schneider, H. Schild and W. Tremel, *Dalton Trans.*, 2011, **40**, 6315.

36 A. Ito, Y. K. Honda, H. Kikkawa, A. Horiuchi, Y. Watanabe and T. Kobayashi, *Cancer. Lett.*, 2004, **212**, 167.

37 A. A. Luderer, N. F. Borrelli, J. N. Panzarino, G. R. Mansfield, D. M. Hess, J. L. Brown, E. H. Bamett and E. W. Hahn, *Radiat. Res.*, 1983, **94**, 190.

38 W. C. Dewey, *Int. J. Hyperthermia.*, 1994, **10**, 457.

39 W. W. He, L. Cheng, L. F. Zhang, Z. Liu, Z. P. Cheng and X. L. Zhu, *Polym.Chem.*,

2014, **5**, 638.

40 N. A. Brusentsov, V. V. Gogosov, T. N. Brusentsov, A. V. Sergeev, N. Y. Jurchenko, A. A. Kuznetsov, O. A. Kuznetsov and L. I. Shumukov, *J. Magn. Magn. Mater.*, 2001, **225**, 113.

41 A. Baeza, E. Guisasola, E. Ruiz-Hernández and M. Vallet-Regí, *Chem Mater*, 2012, **24**, 517.

42 X. Zhang, P. P. Yang, Y. L. Dai, P. A. Ma, X. J. Li, Z. Y. Cheng, Z. Y. Hou, X. J. Kang, C. X. Li and J. Lin, *Adv Funct Mater*, 2013, **23**, 4067.

43 B. Jeong, Y. H. Bae, D. S. Lee and S. W. Kim, *Nature*, 1997, **388**, 860.

44 J. Park, K. An, Y. H. Wang, J. G. Park, H. J. Noh, J. Y. Kim and T. Hyeon, *Nature Materials*, 2004, **3**, 891.

45 B. Jeong, D. S. Lee and J. I. Shon, *J. Polym. Sci. Pol. Chem.*, 1999, **37**, 751.

46 J. Chen, X. Z. Qiu, J. Ouyang, J. M. Kong, W. Zhong and M. M. Q. Xing, *Biomacromolecules*, 2011, **12**, 3601.

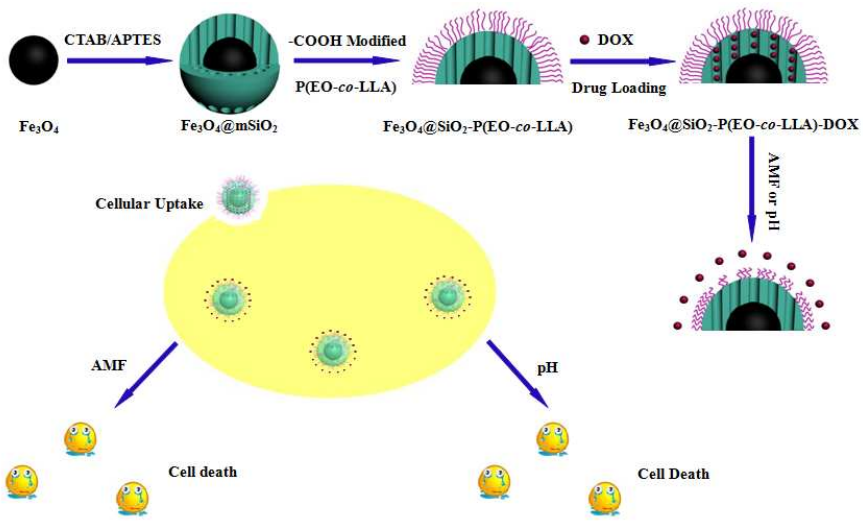

Schematic 1

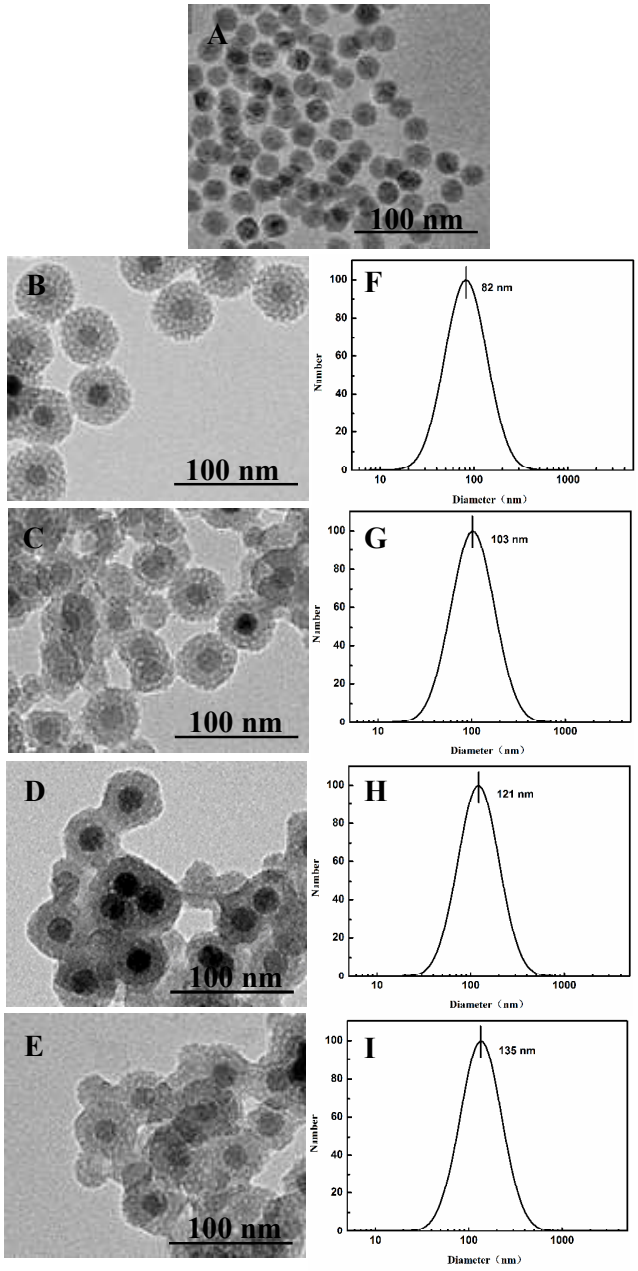

Fig. 1

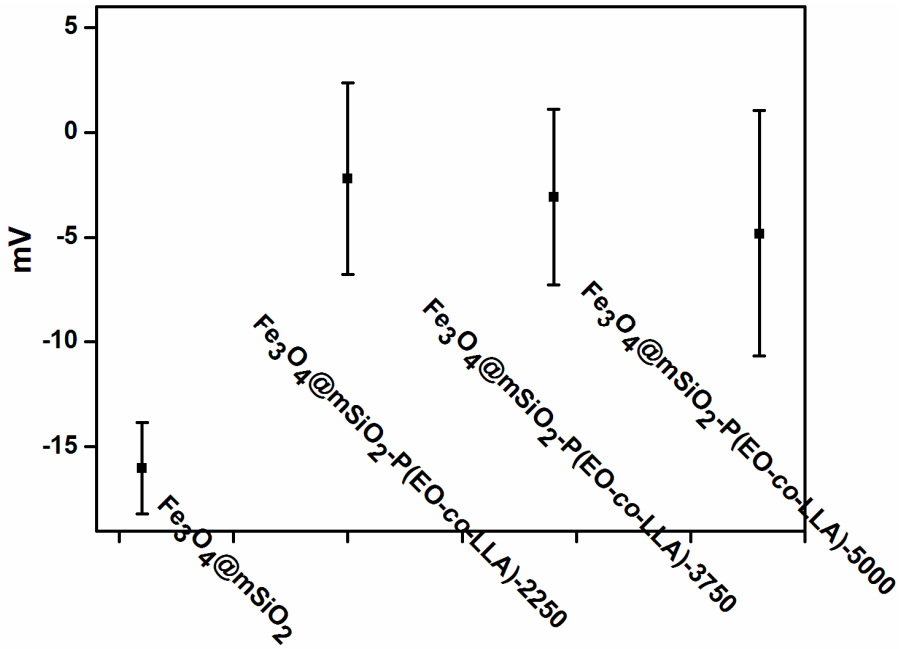

Fig. 2

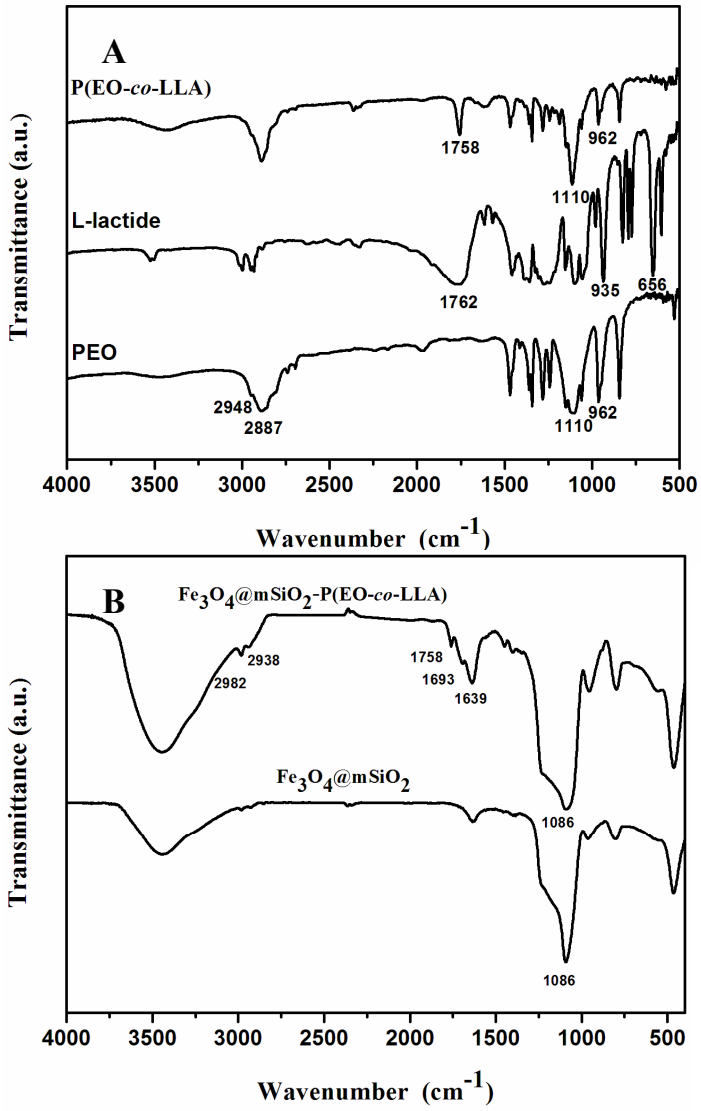

Fig. 3

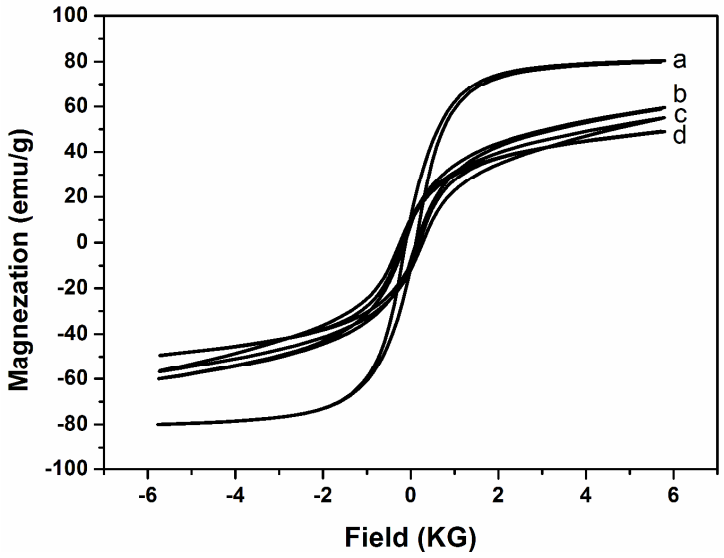

Fig. 4

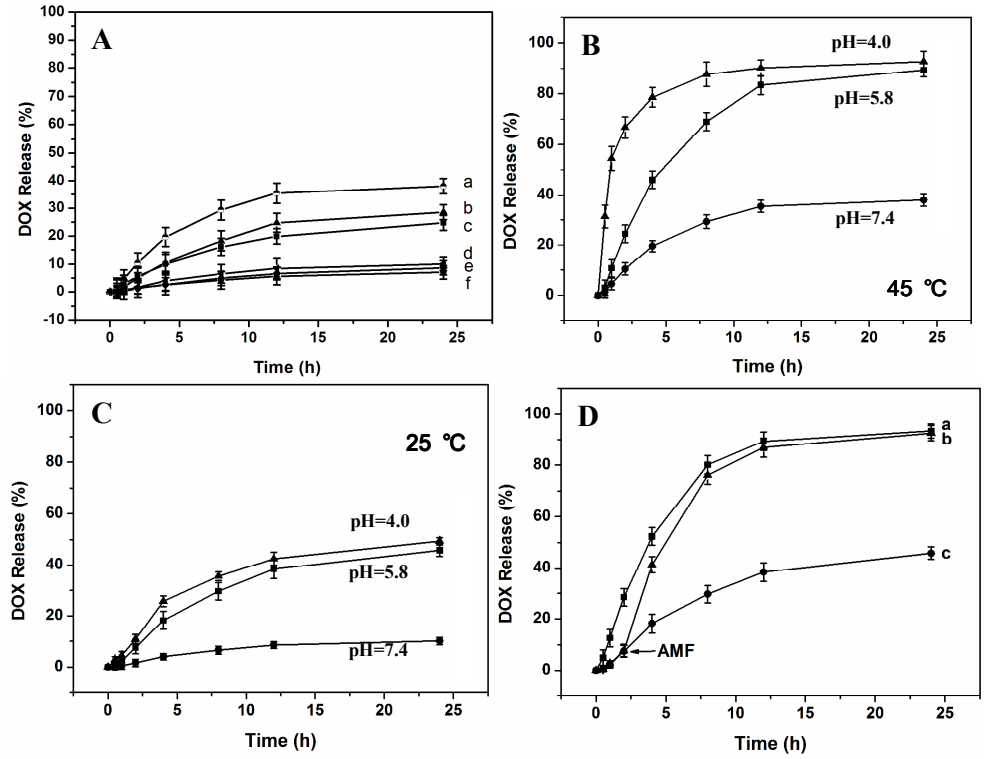

Fig. 5

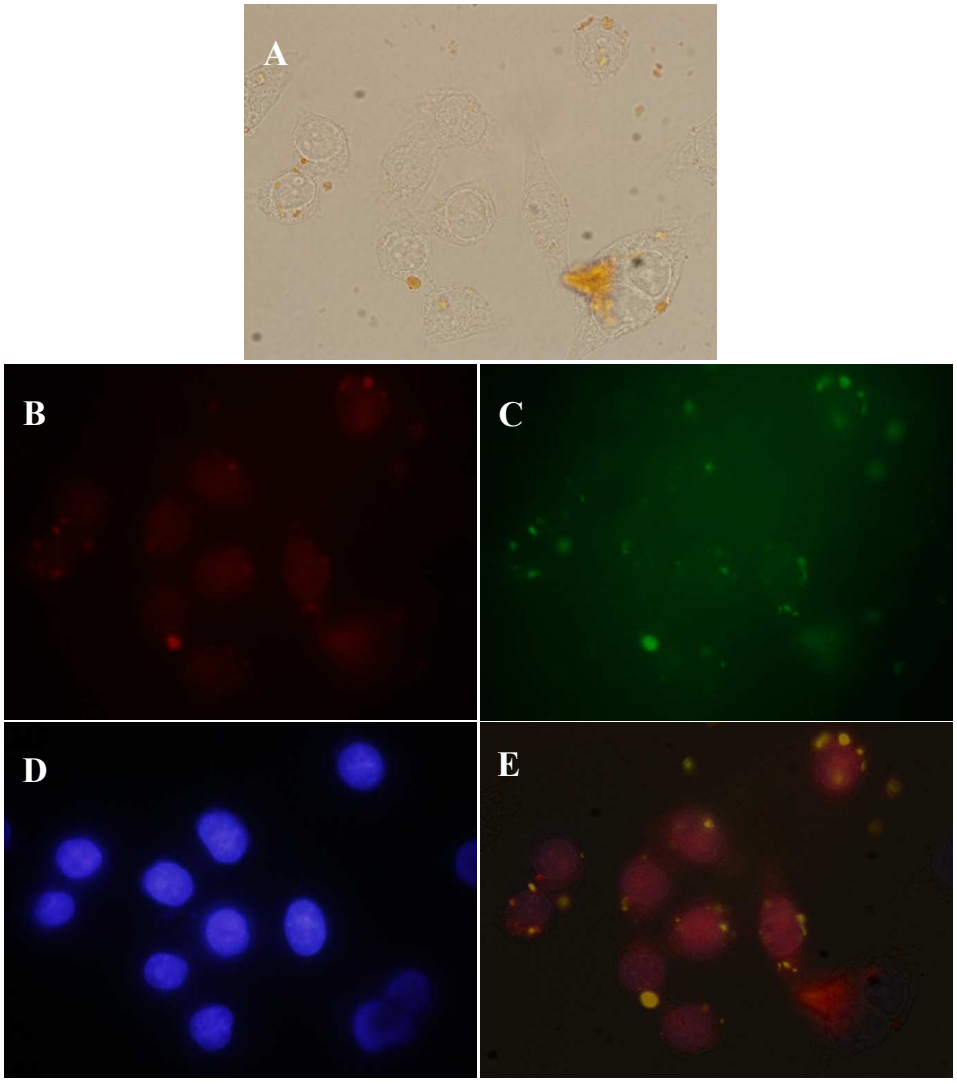

Fig. 6

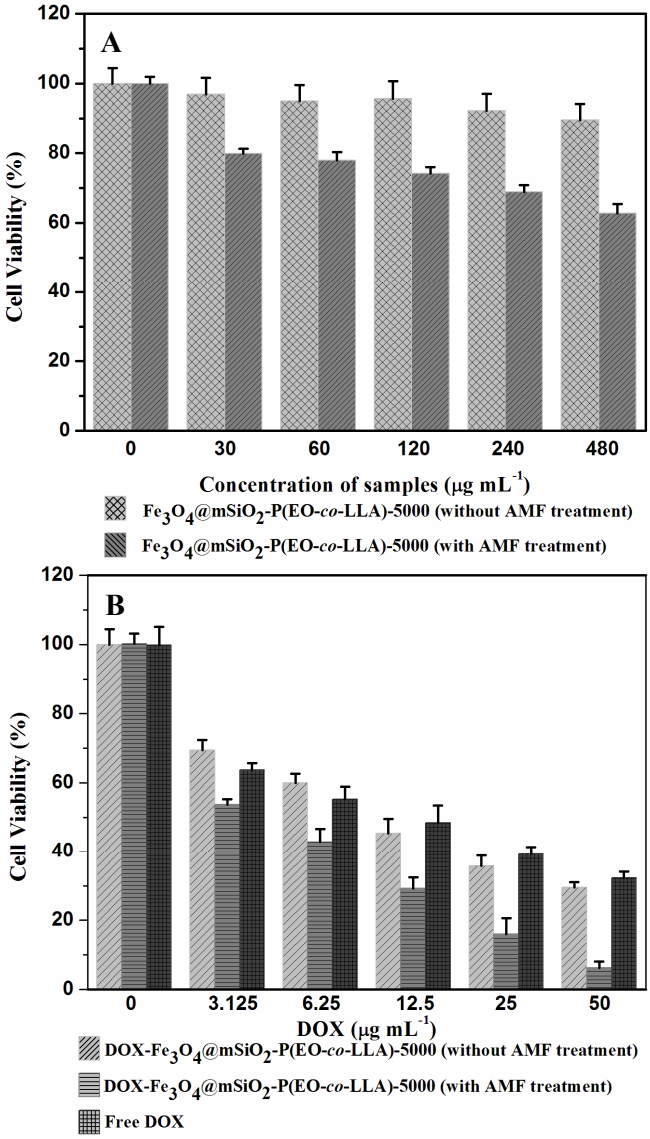

Fig. 7

Table 1 Pore parameters and loading efficiency of the samples

Samples	*BET* ($m^2 g^{-1}$)	V_p ($cm^3 g^{-1}$)	*Pore Size* (nm)	*LE* (%)
Fe_3O_4@$mSiO_2$	326	0.285	2.42	—
DOX-Fe_3O_4@$mSiO_2$-P(EO-*co*-LLA)-2250	152	0.156	2.31	5.9 ± 0.4
DOX-Fe_3O_4@$mSiO_2$-P(EO-*co*-LLA)-3750	100	0.133	2.30	6.2 ± 0.6
DOX-Fe_3O_4@$mSiO_2$-P(EO-*co*-LLA)-5000	68.0	0.095	2.30	6.8 ± 0.5

Table 2 The hydrodynamic size of the samples

Samples	*T=25 ℃*	*T=45 ℃*
DOX-Fe_3O_4@$mSiO_2$-P(EO-*co*-LLA)-2250 （pH 5.8）	97 nm	85 nm
DOX-Fe_3O_4@$mSiO_2$-P(EO-*co*-LLA)-2250 （pH 7.4）	108 nm	102 nm
DOX-Fe_3O_4@$mSiO_2$-P(EO-*co*-LLA)-3750 （pH 5.8）	115 nm	97 nm
DOX-Fe_3O_4@$mSiO_2$-P(EO-*co*-LLA)-3750 （pH 7.4）	130 nm	122 nm
DOX-Fe_3O_4@$mSiO_2$-P(EO-*co*-LLA)-5000 （pH 4.0）	128 nm	99 nm
DOX-Fe_3O_4@$mSiO_2$-P(EO-*co*-LLA)-5000 （pH 5.8）	131 nm	105 nm
DOX-Fe_3O_4@$mSiO_2$-P(EO-*co*-LLA)-5000 （pH 7.4）	149 nm	138 nm

Captions:

Schematic 1. Illustration of the preparation and controlled release process of Fe_3O_4@$mSiO_2$-P(EO-*co*-LLA).

Fig. 1 TEM images of (A) Fe_3O_4, (B) Fe_3O_4@$mSiO_2$, (C) Fe_3O_4@$mSiO_2$-P(EO-*co*-LLA)-2250, (D) Fe_3O_4@$mSiO_2$-P(EO-*co*-LLA)-3750, (E) Fe_3O_4@$mSiO_2$-P(EO-*co*-LLA)-5000 and the hydrodynamic size distribution of (F) Fe_3O_4@$mSiO_2$, (G) Fe_3O_4@$mSiO_2$-P(EO-*co*-LLA)-2250, (H) Fe_3O_4@$mSiO_2$-P(EO-*co*-LLA)-3750, and (I) Fe_3O_4@$mSiO_2$-P(EO-*co*-LLA)-5000.

Fig. 2 Zeta-potential of Fe_3O_4@$mSiO_2$, Fe_3O_4@$mSiO_2$-P(EO-*co*-LLA)-2250, Fe_3O_4@$mSiO_2$-P(EO-*co*-LLA)-3750 and Fe_3O_4@$mSiO_2$-P(EO-*co*-LLA)-5000.

Fig. 3 FTIR spectra of (A) PEO, L-lactide and P(EO-*co*-LLA); (B) Fe_3O_4@$mSiO_2$ and Fe_3O_4@$mSiO_2$-P(EO-*co*-LLA).

Fig. 4 Representative hysteresis-loop measurements of the obtained a: Fe_3O_4@$mSiO_2$, b: Fe_3O_4@$mSiO_2$-P(EO-*co*-LLA)-2250, c: Fe_3O_4@$mSiO_2$-P(EO-*co*-LLA)-3750 and d: Fe_3O_4@$mSiO_2$-P(EO-*co*-LLA)-5000.

Fig. 5 (A) Release profiles of DOX from Fe_3O_4@$mSiO_2$-P(EO-*co*-LLA)-5000, (a: 45℃ and f: 25 ℃), Fe_3O_4@$mSiO_2$-P(EO-*co*-LLA)-3750 (b: 45℃ and e: 25 ℃), Fe_3O_4@$mSiO_2$-P(EO-*co*-LLA)-2250 (c: 45 □ and d:25 □) at pH 7.4. Release profiles of DOX from Fe_3O_4@$mSiO_2$-P(EO-*co*-LLA)-5000 in different pH condition at 45℃ (B) and 25℃ (C), (D) Release profiles of DOX from Fe_3O_4@$mSiO_2$-P(EO-*co*-LLA)-5000 (pH 5.8) a: with AMF from t = 0 h, b: with AMF from t = 2 h, and c: without AMF.

Fig. 6 CLSM images of Hela cells after incubation with 100 μg mL^{-1} of DOX-Fe_3O_4@$mSiO_2$-P(EO-*co*-LLA)-5000 for 6 h. (A) Hella cells (bright), (B) DOX fluorescence in cells (red), (C) FITC labeled DOX-Fe_3O_4@$mSiO_2$-P(EO-*co*-LLA)-5000 (green), (D) Hoechst 33342 labeled cell nucleus (blue), and (E) merged.

Fig. 7 Cell viability of Hela cells incubated with different amount of (A) Fe_3O_4@$mSiO_2$-P(EO-*co*-LLA)-5000, Fe_3O_4@$mSiO_2$-P(EO-*co*-LLA)-5000 with AMF, (B) DOX-Fe_3O_4@$mSiO_2$-P(EO-*co*-LLA)-5000, DOX-Fe_3O_4@$mSiO_2$-P(EO-*co*-LLA)-5000 with AMF, and Free DOX.